AGU ADVANCING EARTH AND SPACE SCIENCE

Geophysical Research Letters®

Key Points:

- Novel satellite laser altimetry techniques map Arctic sea ice deformation at resolutions previously only attainable with airborne lidar
- Surface roughness and pressure ridge sail heights are best represented by exponential normal and log-normal distributions, respectively
- Given the continued loss of older sea ice our results imply an ongoing reduction in ridging intensity, roughness and form drag over time

Correspondence to:

S. L. Farrell,
sineadf@umd.edu

Author Contributions:

Conceptualization: S. L. Farrell
Data curation: K. Duncan
Formal analysis: K. Duncan, S. L. Farrell
Funding acquisition: S. L. Farrell
Investigation: K. Duncan, S. L. Farrell
Methodology: K. Duncan, S. L. Farrell
Project Administration: S. L. Farrell
Resources: S. L. Farrell
Software: K. Duncan
Supervision: S. L. Farrell
Validation: K. Duncan, S. L. Farrell
Visualization: K. Duncan, S. L. Farrell
Writing – original draft: S. L. Farrell

Determining Variability in Arctic Sea Ice Pressure Ridge Topography With ICESat-2

K. Duncan[1] and **S. L. Farrell[2]**

[1]Earth System Science Interdisciplinary Center, University of Maryland, College Park, MD, USA, [2]Department Geographical Sciences, University of Maryland, College Park, MD, USA

Abstract We investigate the characteristics and distribution of pressure ridges in Arctic sea ice using a novel algorithm applied to ICESat-2 surface heights. We derive the frequency and height of individual pressure ridges and map surface roughness and ridging intensity at the basin scale over three winters between 2019 and 2021. Comparisons with near-coincident airborne lidar data show that not only can we detect individual ridges 5.6 m wide, but also measure sail height more accurately than the existing ICESat-2 sea ice height product. We find large regional variability in ridge morphology not only related to parent ice type but also geographic location. Ridge sails are best represented by log-normal distributions while surface roughness is well fit by an exponential normal function. Our results reveal that high-resolution satellite altimetry is valuable for characterizing sea ice deformation at short length-scales and delivers observations that will advance ridging parameterizations in sea ice models.

Plain Language Summary Pressure ridges, a result of convergence and deformation between ice floes, restrict the movement of air across sea ice and pose an impediment to transport across or through the ice. The laser altimeter on ICESat-2 provides height measurements of sea ice surface topography every 0.7 m in the direction of flight, from which we calculate surface roughness and measure the sail height and frequency of pressure ridges across the Arctic. We use coincident aircraft-mounted lidar data to evaluate the accuracy of ridge topography derived from ICESat-2. Our methods accurately distinguish ridges and reproduce sea ice deformation statistics at an along-track resolution previously only attainable from airborne platforms. We find that while year-to-year variability in pressure ridge morphology is low, regional variations are significant. Consistent with previous studies, we find distinct deformation characteristics depending on the age of the ice. Because the oldest ice in the Arctic continues to decline our results imply a reduction in surface roughness and ridging intensity over time, lowering form drag across the ice surface. Our study demonstrates that high-resolution satellite altimeter observations can be used to derive detailed measurements of sea ice topography that will ultimately support process studies and advances in sea ice modeling.

1. Introduction

The advent of high-resolution satellite laser altimetry permits for the first time a complete mapping of sea ice surface topography at the basin scale. The Advanced Topographic Lidar Altimeter System (ATLAS) on ICESat-2 has a 10 kHz pulse repetition frequency and a footprint diameter of ∼11 m (Magruder et al., 2020) resulting in ∼0.7 m along-track sampling of Earth's surface (Markus et al., 2017). This configuration is ideal for mapping rough sea ice in high fidelity, allowing us to resolve individual ice floes, pressure ridges and leads at meter-scale (Farrell et al., 2020). ICESat-2's continual data acquisitions advance our capabilities for observing ice deformation compared to previous techniques, including airborne laser profiling (e.g., Dierking, 1995; W. D. Hibler et al., 1974; Lowry & Wadhams, 1979; Tan et al., 2012; Wadhams et al., 1992), upward looking and side scan sonar (e.g., Davis & Wadhams, 1995; W. D. Hibler et al., 1972), autonomous underwater vehicles (e.g., Wadhams & Doble, 2008), airborne electromagnetic induction techniques (Haas et al., 2009), and in situ observations (e.g., Strub-Klein & Sudom, 2012; Timco & Burden, 1997), that were each spatiotemporally limited. Leveraging ICESat-2's widespread observations, we extract the morphological characteristics of sea ice ridges across the Arctic Ocean and examine variations in both surface roughness and ridging as a function of geographical area.

Pressure ridges formed by ice convergence increase ice thickness and impact atmospheric flow across the surface thus modifying the momentum flux from the atmosphere through the ice to the ocean (Arya, 1973). Defined as a wall of broken ice forced up by pressure (WMO, 1970), ridges can be "fresh" (i.e., a first-year ridge) or

"weathered and old." Pressure ridges in isostatic equilibrium mature to have roughly triangular sails with rounded crests (Parmerter & Coon, 1972). Early submarine observations revealed an uneven distribution of ridging across the Arctic with the heaviest deformation found north of Greenland and Canada (e.g., Bourke & McLaren, 1992; W. D. Hibler et al., 1974).

Ice roughness accumulates, and persists, throughout the growth season. Depending on its location and roughness, ice can potentially survive dissipation through melt or advection, leading to further deformation and roughening in subsequent seasons. Multiyear ice that has survived at least one summer is hence rougher than first-year ice (Wadhams & Toberg, 2012), and roughness influences the location and fraction of summer melt ponds (Eicken et al., 2004). Knowledge of sea ice topography is necessary to parameterize momentum transfer to the ocean in numerical simulations since surface stress increases with surface roughness (Martin et al., 2016; Tsamados et al., 2014). Metrics on ice ridging are also required to model the design load of sea ice on marine structures (Timco & Burden, 1997) and the scattering of under-ice acoustics (Wadhams & Toberg, 2012). Tsamados et al. (2014) found a net decline in ice thickness, area and velocity when roughness was included in a model simulation. The representation of ice surface roughness and its variability due to the sustained, multi-decadal loss of older Arctic ice (Perovich et al., 2019) remains however inadequate in sea ice models (Martin et al., 2016).

Sea ice roughness (σ_h) is used here as a general term to describe all sources of ice deformation through ridging, rafting and rubbling, and includes hummocks as well as wind-driven undulations on the ice surface due to snow-drifts and sastrugi and is defined as the standard deviation of surface elevation. But, ICESat-2 also has the capability to directly observe ice deformation at the scale of the individual pressure ridge due to its dense along-track sampling (Farrell et al., 2020). We can therefore retrieve ridge morphology as well as σ_h. We characterize the upper expression of pressure ridges (sails) to obtain estimates of sail height (H_S) as well as ridge width (W_R), spacing (D_R) and intensity (I_R). Building upon an initial feasibility study of σ_h in April 2019 (Farrell et al., 2020), we investigate regional variations in H_S, D_R and I_R as well as σ_h at the end of winter (April) spanning three years between 2019 and 2021. Results represent deformation accumulated throughout the winter period and hence include both fresh and weathered ridges. We analyze ridge morphology at length scales ranging from individual floes to regional-scale deformation and upwards to the full basin scale, providing pan-Arctic metrics. Statistical models fit to the observations describe the characteristic shapes of the derived ridge dimensions in two regions with distinct deformation histories. Findings are validated via comparison with Operation IceBridge (OIB) lidar data collected during under-flights of ICESat-2 in April 2019.

2. Data and Methods

2.1. ATL03

ATLAS (operating at 532 nm) obtains multibeam surface height profiles of the air/snow interface with respect to the reference ellipsoid (see e.g., Kwok, Markus, et al., 2019). The ICESat-2 ATL03 global geolocated photon height data product (Neumann et al., 2021) is designed to be a single source for all photon data and ancillary information needed for higher-level ICESat-2 data processing. ATL03 contains the latitude, longitude and height (h_{ph}) relative to the WGS-84 ellipsoid of all photons downlinked by the ATLAS instrument (see Neumann et al., 2019).

2.2. ATL07

The ICESat-2 ATL07 sea ice height data product (Kwok et al., 2021) is derived from the ATL03 product. It contains sea ice and lead heights, adjusted for geoid and tidal variations and inverted barometer effects. It is calculated using fixed 150-photon height aggregates in segments with variable lengths in the along-track direction ranging from ∼27 to 200 m and a height precision of ∼0.02 m over flat surfaces such as leads (Kwok, Markus, et al., 2019).

2.3. Ridge Detection

The number of photons recorded by the ATLAS detector depends on both the morphology and reflectance of Earth's surface. Detections comprise photons scattered from the surface (signal) and background (noise) photons, including from solar background, detector noise and atmospheric scattering. The separation of background from surface photons is thus a critical step in the retrieval of accurate surface height profiles.

Kwok, Kacimi, et al. (2019) report that the ATL07 algorithm does not capture sea ice height variability at short length-scales in areas of high surface roughness where pressure ridges are present. Since our goal is to retrieve ridge topography, we therefore apply a novel method that takes advantage of the full-resolution geolocated photon heights in the ATL03 product. The University of Maryland-Ridge Detection Algorithm (UMD-RDA) is designed to extract sea ice surface height, h, from ATL03 data. Over sea ice, the ATL03 photon cloud provides photon heights (h_{ph}) in a 30 m vertical range window about the surface. We construct a h_{ph} height distribution using vertical bins of 0.5 m and 5-shot aggregates of photons (~2.8 m in along-track distance). Photons clustered around the mode of this h_{ph} distribution indicate the surface return and these are retained. If the h_{ph} distribution is bimodal, with modes in consecutive vertical bins, the lowest mode indicates the surface mode (h_m). For bimodal h_{ph} distributions with modes that do not occur in consecutive bins, modal heights are compared with those of the previous shot and the mode closest to the previous modal height is selected. Only photons within the range ($h_m + 10$ m) $\geq h_{ph} \geq (h_m - 2$ m) are retained so as to adequately capture h_{ph} of ridge sails and leads, respectively. All other photons are considered background and are discarded. To reduce any remaining background photons from the final derivation of h, photons are further downselected, retaining only those within the 15th–85th percentiles of the h_{ph} distribution. Sea ice surface height (h) is defined as the 99th percentile of the remaining h_{ph} distribution and indicates the retrieval arising from the air/snow interface, that is, the first surface interface encountered by the laser pulse.

UMD-RDA surface finding is applied on a per-shot basis to retain h at an along-track resolution of ~0.7 m and has a height precision of ~0.01 m over flat surfaces such as leads (Farrell et al., 2020). UMD-RDA height estimates are only processed where ATL07 data are available (Kwok et al., 2021) thus eliminating cloud-contaminated retrievals. Atmospheric, tide, and mean sea surface (MSS) geophysical height corrections are applied to h so as to obtain corrected heights (h_c) relative to the MSS. Here we use the Technical University of Denmark 2018 Mean Sea Surface (DTU18 MSS) model (Andersen et al., 2018). Ice surface roughness (σ_h) is estimated by taking the standard deviation of h_c in 25 km along-track segments for all cloud-free ICESat-2 sea ice data north of 65°N. The σ_h metric captures the surface topography of all floating morphological features of the ice cover observed by ICESat-2 including ridges, rafts, rubble fields and hummocks as well as sastrugi and snowdrifts.

Next, the morphological characteristics of individual ridge sails on the ice surface are determined. The local level ice surface (H_L) is computed as the mode of the h_c height distribution in 25 km along-track segments. In segments with a large percentage of leads, the h_c distribution can be bimodal. In these cases, the highest modal elevation defines H_L. So as to extract ridge heights, all estimates of h_c are converted to height anomalies (h_a) relative to H_L. Since our goal here is to detect and characterize pressure ridges, we set an optimal cutoff height (H_0) above H_L, that defines the minimum ridge height (Lowry & Wadhams, 1979). H_0 is selected based on the expected snow and ice deformation conditions and mitigates against the effect of erroneously including sastrugi and snow dune heights in the sail height calculation. Following W. D. Hibler et al. (1972), Tan et al., 2012 and Duncan et al. (2018), we set $H_0 = 0.6$ m to differentiate ridge sails from snow features (Newman et al., 2014). Independent ridges are defined using the Rayleigh criterion where the local maximum (peak) is at least twice as high as the neighboring minima (troughs) on both sides and the minima descend at least halfway toward H_L (Lowry & Wadhams, 1979; Tan et al., 2012). Ridges can therefore comprise multiple sails, and two adjacent topographical elements must fulfill the Rayleigh criterion to be resolved as separate ridge elements (Castellani et al., 2014). H_s is the maximum sail height of a ridge relative to H_L (i.e., the maximum h_a within the ridge element). Following Timco and Burden (1997), ridge width (W_R) is the along-track distance between the points of intersection of H_L and the neighboring minima on either side of the ridge peak. Ridge spacing (D_R) is the peak-to-peak distance between consecutive H_S maxima. The latter two metrics will be impacted by the angle of intersection between the ICESat-2 orbit and the ridge orientation, but assuming heterogeneity in ice surface conditions across the Arctic, metrics should be robust at the basin scale.

2.4. Validation Data

ICESat-2's capabilities to measure ice topography in high resolution are quantified through comparisons of both the UMD-RDA and ATL07 sea ice heights with coincident aircraft observations from the Airborne Topographic Mapper (ATM) lidar (Studinger, 2013) collected during under-flights of ICESat-2 in April 2019 as part of NASA's OIB campaign (MacGregor et al., 2021). Kwok, Kacimi, et al. (2019) found that ATM and ATL07 surface heights were highly correlated when ATM data were averaged at the ATL07 segment length
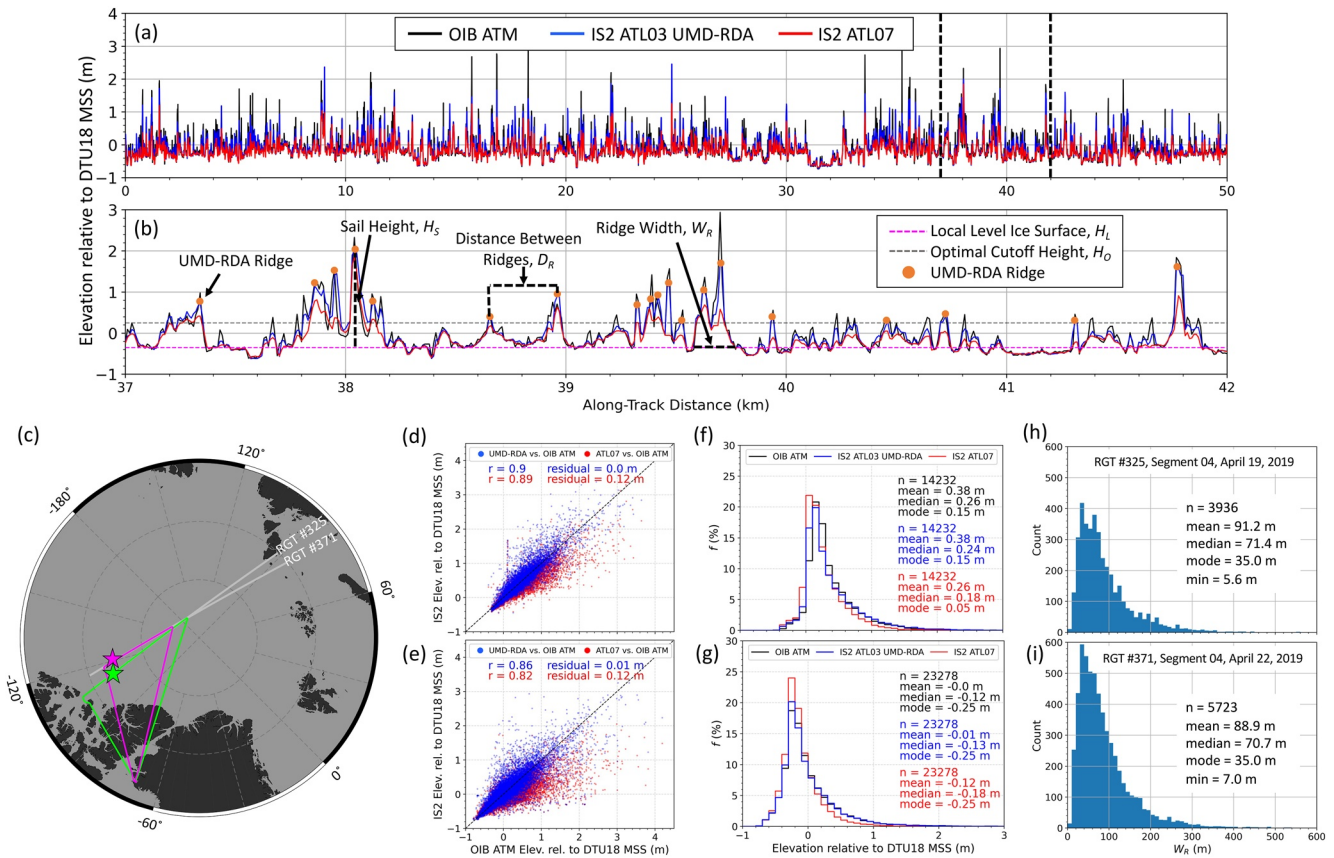
Figure 1. Arctic sea ice topography from ICESat-2. (a) Operation IceBridge (OIB) Airborne Topographic Mapper (ATM) lidar (black), ICESat-2 ATL03 University of Maryland-Ridge Detection Algorithm (UMD-RDA) (blue) and ATL07 (red) sea ice height profiles along a 50 km transect across multiyear sea ice (magenta star in c) on 22 April 2019. (b) A close-up 5-km view (section between vertical black dashed lines in a) illustrating surface topography and pressure ridge metrics defined in the text. (c) Map showing OIB flights on 19 (green) and 22 (magenta) April 2019, with segment 04 of ICESat-2 reference ground tracks (RGTs) 325 and 371 (gray lines) and the locations of coincident validation data collection (stars). (d, e) Scatterplots comparing UMD-RDA (blue dots) and ATL07 (red dots) with coincident OIB ATM height measurements on 19 and 22 April 2019, respectively. (f, g) Sea ice surface height distributions for coincident OIB ATM (black), UMD-RDA (blue), and ATL07 (red) data on 19 and 22 April 2019, respectively. (h, i) Ridge width distributions derived from ALT03 UMD-RDA segment 04 of RGTs 325 and 371, respectively.

scale (∼27–200 m) and manually coregistered. Larger differences were however found in areas of rough sea ice, when the ATL07 algorithm was unable to capture the full height distribution due to the segment-based approach (Kwok, Kacimi, et al., 2019).

Here we examine observations from two underflights that had spatiotemporal coincidence with ICESat-2 orbits and were conducted with small time differences (<38 min) to minimize ice drift between the airborne and satellite acquisitions (Kwok, Kacimi, et al., 2019). On 19 April 2019, ∼142 km of coincident validation data were collected below ICESat-2 reference ground track (RGT) 325, while on 22 April 2019 coincident data spanning ∼233 km were collected below RGT 371. ATM is a conically-scanning lidar (Krabill et al., 2002) and samples the ice surface unevenly (Duncan et al., 2018). We investigated the averaging length best suited for validation of the finer-scale ICESat-2 observations (Duncan & Farrell, 2020), and here ATM data are extracted along the ICESat-2 height profiles using a nearest neighbor mean with $n = 5$. UMD-RDA, ATL07, and ATM height profiles relative to the DTU18 MSS are sampled at 10 m along-track increments for direct comparison.

3. Kilometer-Scale Topography

First, we examine sea ice height at the floe scale O(1–10 km), comparing measurements of h_c derived from ATM, ATL07, and the UMD-RDA (Figure 1). The validation site (Figure 1c) comprised old, thick ice (Perovich et al., 2019). The height variability of this heavily deformed surface (Figure 1a) is captured by all three methods. At the km-scale (Figure 1b) we can see both individual small ridges with a typical triangular shape in cross-section

as well as the structure of ridge complexes, with multiple sails and irregular height profiles. Pressure ridge (H_s, W_R, D_R) and surface topography metrics (H_L and H_0) described in Section 2.3 are illustrated in Figure 1b.

Comparisons against ATM data show that the ATL07 algorithm acts as a low-pass filter, underestimating the height of individual ridge sails (red curves, Figures 1a and 1b), consistent with previous studies (Kwok, Kacimi, et al., 2019). Despite this, ATL07 and ATM heights are strongly correlated ($r \geq 0.82$, red dots, Figures 1d and 1e). ATL07 heights are however biased low by ∼0.12 m, with median height underestimated by 0.06–0.08 m (Figures 1f and 1g). The largest differences are associated with rougher ice topography (Figures 1d–1g).

UMD-RDA is designed to resolve individual ridges and the resulting height distributions are strongly correlated with ATM heights ($r \geq 0.86$, blue dots, Figures 1d and 1e). ATM and UMD-RDA mean, median and modal heights differ by ≤0.02 m (Figures 1f and 1g). Examining UMD-RDA heights across the central Arctic (ATL03 segment 04, Figures 1c), 3936 ridges are detected on RGT #325, and 5723 on RGT #371. The narrowest ridge resolved by the UMD-RDA is 5.6 m wide. Modal ridge width is 35 m, and median and mean widths are ∼71 and ∼90 m, respectively (Figures 1h and 1i).

4. Interannual Variability at Pan-Arctic Scales

To investigate the regional gradients in ice roughness and their interannual variability, σ_h in April 2019–2021 is mapped at 1/4° across the Arctic Ocean (Figure 2). Histograms of σ_h (insets, Figure 2) show little change in mean σ_h during the 3-year period, which ranges 0.25–0.27 m. The maps however illustrate the dichotomy in σ_h between ice types, where the convergent ice regimes north of Greenland and Ellesmere Island result in the majority of multiyear ice with $\sigma_h \geq 0.3$ m, while first-year ice has $\sigma_h \leq 0.2$ m. Figure 2 also reveals of export of multiyear ice through the Fram Strait and advection of multiyear ice through the southern Beaufort Sea, which was particularly prevalent in 2021.

Extending the analysis to the derived ridge metrics provides further insight into the state of the sea ice cover and the year-to-year variations in Arctic ice deformation. Here, H_{Smax} is the maximum H_S per kilometer, while D_R is defined as the mean ridge spacing per 10 km. As with σ_h, these data are also mapped to a 1/4° grid. Regional variability in D_R does not directly map to H_{Smax} and hence a metric combining these variables is useful. Ridging intensity (I_R), first introduced by W. D. Hibler et al. (1974), is easily derived from laser profiling data and is defined as the mean sail height multiplied by the sail frequency per kilometer (i.e., $I_R = <H_S>/<D_R>$, where $<H_S>$ is mean sail height and $<D_R>$ is mean spacing). I_R is proportional to aerodynamic form drag of pressure ridges (Arya, 1973; Dierking, 1995). Figure 2 reveals that I_R is correlated with σ_h. Both metrics indicate localized ridged ice along the Siberian coastline, particularly in the Chukchi and East Siberian Seas possibly due to convergence against a land boundary or land-fast sea ice.

5. Regional-Scale Ice Deformation

Bridging between the kilometer and pan-Arctic scales (Figures 1 and 2, respectively) we analyze ICESat-2 data at the intermediate scale O(10–100 km), relevant to the typical resolution of climate models (Hunke et al., 2010). Pressure ridge distributions from two parts of the Arctic Ocean are compared: north of the Canadian Arctic Archipelago (region A) and within the Beaufort Gyre (region B). These two distinct regions were defined by examining the geographical distribution of σ_h between April 2019 and 2021: region A encompasses older, rougher, multiyear sea ice while B contains younger, smoother, predominantly first- and second-year ice as indicated by the location of ice aged 2 years and older (solid contour, Figure 2, top row). Their areas are equivalent so as to maintain an equal number of observations between the two regions.

We calculate the distributions of σ_h, H_{Smax}, and D_R in A and B and test a range of analytical functions (normal, log-normal, log-logistic and exponentially modified Gaussian) to investigate the best statistical fits to the distributions. The regional results (Figure 3) show that all distributions have exponential tails denoting the fraction of pressure ridging present. Although physical deformation processes are fundamentally the same in both regions, differences in ice deformation between the two are however apparent due to the period over which ridging occurs. In region A, average σ_h was ∼0.4 m but decreased by 0.04 m over the 3-year period (Figure 3a), while in B, mean and modal σ_h remained approximately constant at ∼0.2 m during the study period (Figure 3g). Surface height variability was larger in A and the standard deviation of σ_h was approximately double that of ice in B (Figures 3a
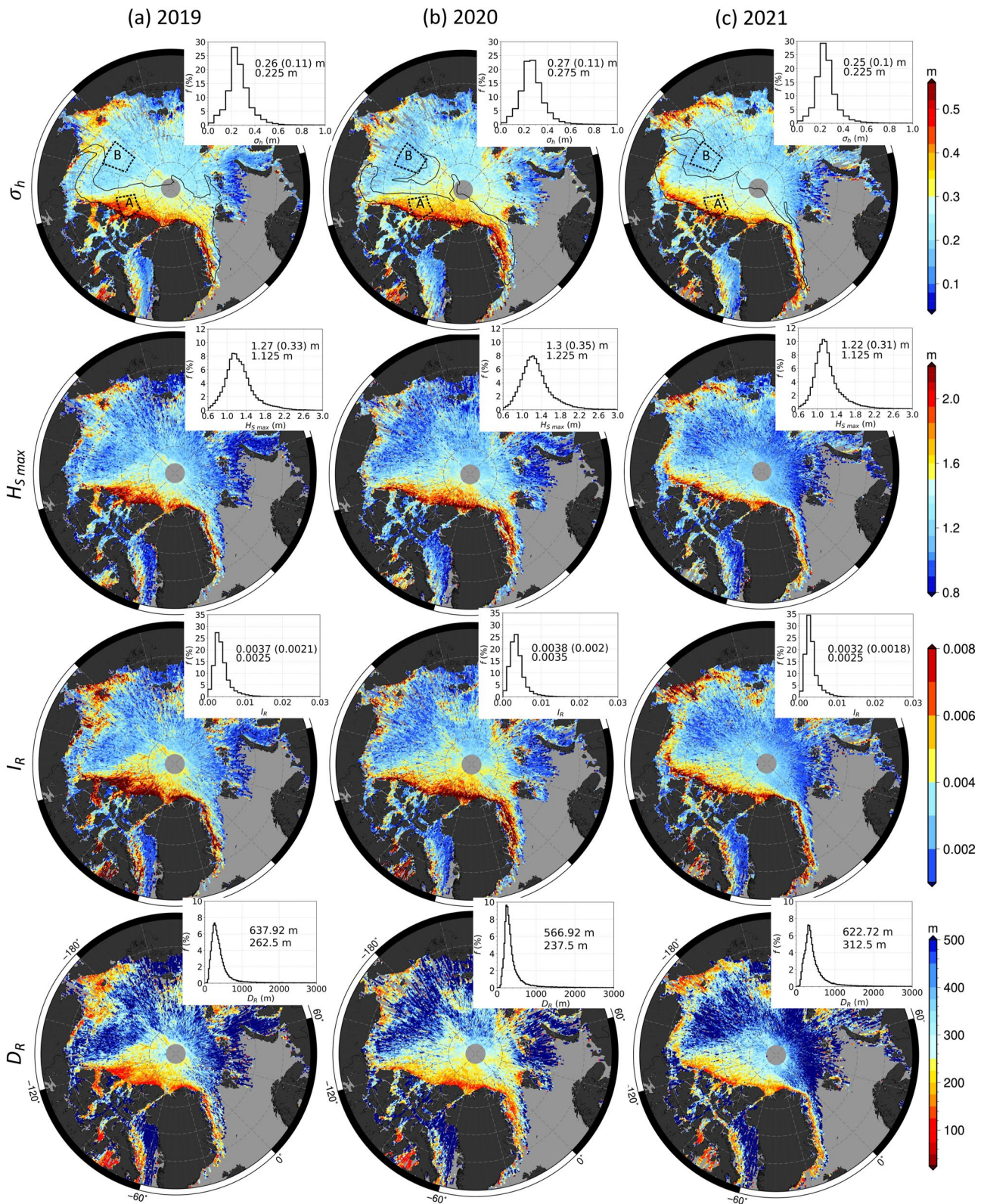
Figure 2. Pan-Arctic maps of surface roughness (σ_h), maximum sail height (H_{Smax}), ridge intensity (I_R), and distance between ridges (D_R) in April (a) 2019, (b) 2020 and (c) 2021. Insets show distributions with mean (standard deviation) and modal statistics provided to the right of each histogram. Dashed black lines (top row) outline the locations (A, B) of the regional analysis. Solid black contours (top row) outline the location of ice aged 2 years and older (from M. Tschudi et al., 2019).
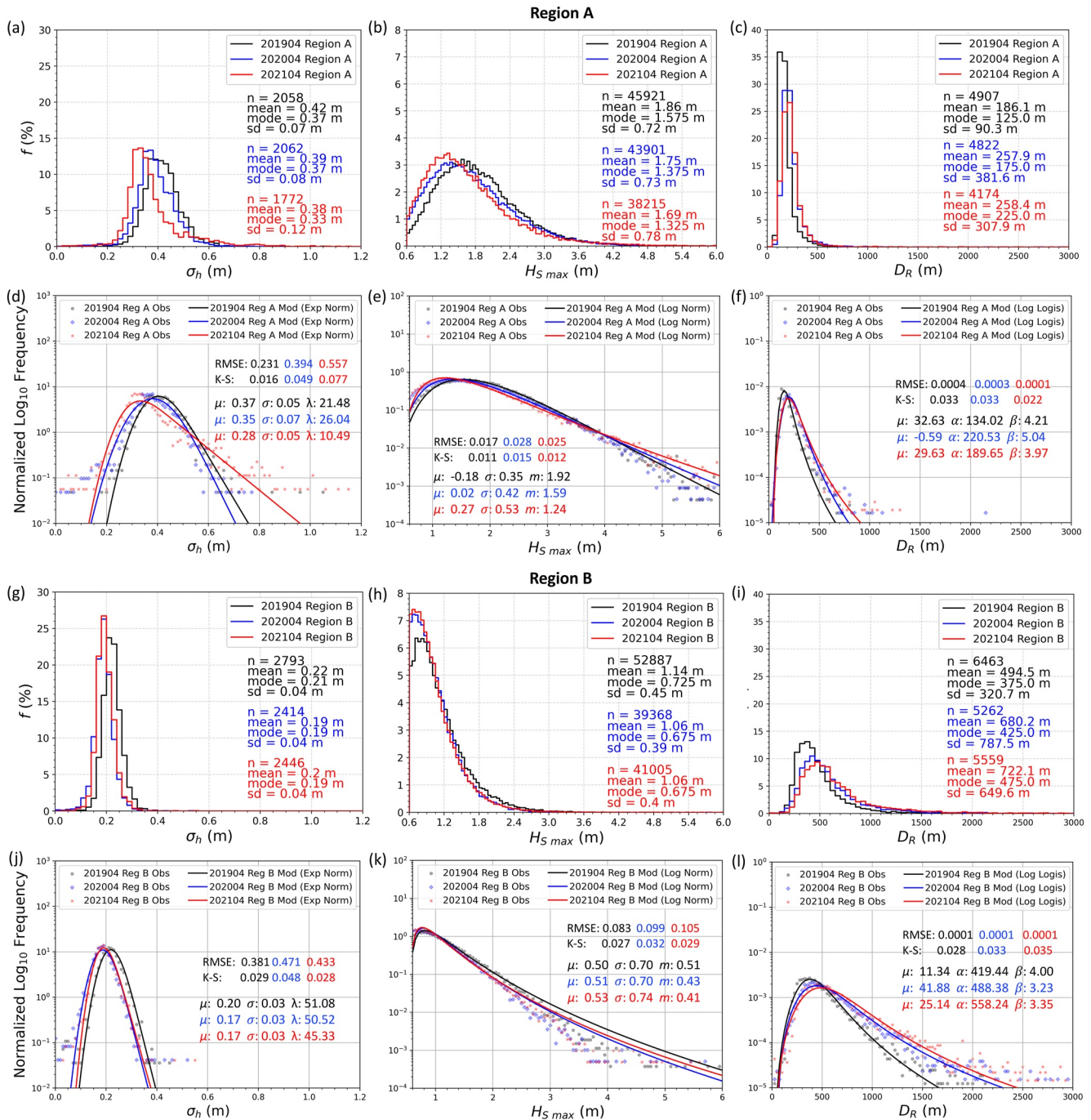
Figure 3. Statistical analysis of surface roughness (σ_h), maximum sail height (H_{Smax}) and distance between ridges (D_R) in April 2019 (black), 2020 (blue) and 2021 (red) for regions A (a–f) and B (g–l). Distributions of σ_h, H_{Smax} and D_R with the number of observations (n) and their mean, mode and standard deviation (sd) are shown on rows 1 and 3, for regions A and B, respectively. Semi-log plots of σ_h, H_{Smax} and D_R ("Obs", black, blue and red dots) and the associated model ("Mod") fits (solid lines) are on rows 2 and 4, for regions A and B, respectively. Root-mean-square error, Kolmogorov–Smirnov (K–S) test statistics and the best-fit model parameters are shown to the right of each distribution.

and 3g). The elongated tail of the H_{Smax} distribution in A (Figure 3b) reveals that sails are frequently thicker than 3 m in older ice, but we find that this is rare in younger ice (region B, Figure 3h). Roberts et al. (2019) demonstrated theoretically that deformation of the ice cover seldom includes the later stages of ridging and showed that most sea ice is minimally crushed when the pack is compressed. Roberts et al. (2019) posit that this is because it is energetically preferable to form many small ridges rather than few large ridges. Our data confirm this prediction

illustrating that smaller ridges are more common across the ice cover than very large, pressure ridge complexes (Figures 3b and 3h). H_{Smax} in the older ice of region A averaged 0.63–0.72 m higher than in B and modal H_{Smax} in A was approximately double that of region B (Figures 3b and 3h). 5% of sails in A were ≥3.12 m, with 1% of sails ≥4 m. Conversely 95% of all sails in B were ≤2 m. Ridge sails were 2.6–2.8 times further apart in B than in A, with modal D_R of 375–475 m in B compared to 125–225 m in A (Figures 3c and 3i).

The non-Gaussian nature of the sea ice surface height distribution is demonstrated in Figures 3d and 3j, where σ_h observations are well fit by an exponential normal (exponentially modified Gaussian) model in both regions, though the positively skewed surface topography is more evident in A, the older ice zone. The statistical distribution of H_{Smax} in A is best represented by a log-normal distribution (Figure 3e) and the tail is almost straight on the semi-log axis, indicating a negative exponential. The H_{Smax} distribution in B has not however acquired a fully negative exponential tail, and these data were also well represented by a Weibull distribution (not shown). Previous studies have shown D_R follows a log-normal distribution (e.g., Davis & Wadhams, 1995; Dierking, 1995). Our observations of D_R are best fit by a log-logistic distribution in both regions (Figures 1 and 3f) similar in shape to a log-normal distribution, but with heavier tails. The results show a slight increase in D_R in both regions between April 2019 and 2021 suggesting less frequent ridging over time.

6. Discussion

ICESat-2 measurements of ice surface topography can reproduce sea ice deformation statistics at a resolution previously only attainable from aircraft surveys. Sea ice surface roughness (σ_h), sail height (H_{Smax}), ridge width (W_R), spacing (D_R) and intensity (I_R), measured at the end of winter between 2019 and 2021, yielded good coverage across a range of ice types and deformation regimes in the Arctic Ocean. We investigated ridge topography at a range of length scales O(0.01–1,000 km). Consistent with previous studies (e.g., Bourke & McLaren, 1992; W. D. Hibler et al., 1974) we found ice deformation is much more prevalent in multiyear than in seasonal ice. Our results also confirm that deformation varies not only with ice regime, but also geographic location. Both H_{Smax} and I_R were greatest along the land boundaries of the multiyear ice zone and were a factor of two larger than the deformation characteristics of multiyear ice at more northerly latitudes in the central Arctic. Localized deformation in the seasonal ice zone, due to convergence against a static boundary, can result in areas with I_R commensurate with that found in multiyear ice. The topographic variability of all snow and ice deformation features observed by ICESat-2 was captured by σ_h and observations were best fit by an exponential normal function demonstrating the non-Gaussian characteristics of sea ice topography. H_{Smax} was however better represented by a log-normal distribution in both rough and smooth ice regimes, and H_{Smax} was >60% larger in the roughest ice zone with little interannual variability across the 3 years studied. In the smoother ice zone, D_R was 2–3 times greater than in the rougher ice. H_{Smax} and I_R were lower overall in April 2021 than in 2019 and 2020, especially in the Eurasian Basin.

Evaluating against the published literature we believe this is the largest ice deformation data set (Duncan & Farrell, 2022) of its kind created to date. The ongoing availability of ICESat-2 data means regional deformation events and variability in σ_h, H_S, D_R and I_R can be monitored year-round. Pressure ridge characteristics such as H_S, D_R and I_R are necessary to model form drag but this information remains lacking in many Earth system models (Martin et al., 2016; Roberts et al., 2019; Tsamados et al., 2014). Martin et al. (2016) showed that models also lack a complete representation of feedbacks between ice roughness, thickness, drift and deformation, limiting our ability to predict how atmosphere-ice-ocean momentum transfer varies with time. ICESat-2 delivers observations of both individual pressure ridges at short length scales and σ_h, H_S, D_R and I_R at the basin scale thereby providing the needed ice deformation statistics to advance sea ice parameterizations.

First-year ice now comprises ∼70% of the Arctic ice cover compared to 35%–50% in the 1980s (Perovich et al., 2019). With the continued loss of the oldest ice (M. A. Tschudi et al., 2020) the Arctic is rapidly transitioning to a predominantly first-year ice cover. In the future ice topography will become dominated by the characteristics of pressure ridges formed in first-year ice (Wadhams & Toberg, 2012). The sustained loss of multiyear ice, coupled with our basin-scale results, implies a decline in H_S, an increase in D_R, and an on-going reduction in I_R and hence form drag over time. Long-term and widespread observations of ice deformation from ICESat-2 will improve our understanding of how sea ice moderates the momentum flux between the atmosphere and ocean, providing a more complete picture of how and why the ice regime of the Arctic Ocean is transforming.

Data Availability Statement

NASA ICESat-2 ATL03 and ATL07 sea ice height data are at https://doi.org/10.5067/ATLAS/ATL03.005 and https://doi.org/10.5067/ATLAS/ATL07.005, respectively. NASA ATM data are at https://doi.org/10.5067/19SIM5TXKPGT. Sea ice age data are at https://doi.org/10.5067/UTAV7490FEPB. The DTU18 MSS is at https://ftp.space.dtu.dk/pub/DTU18/. Processed sea ice pressure ridge sail data described in this study are available at https://doi.org/10.5281/zenodo.6772544.

References

Andersen, O. B., Rose, S. K., Knudsen, P., & Stenseng, L. (2018). *The DTU18 MSS mean sea surface improvement from SAR altimetry*. Technical University of Denmark. Retrieved from https://ftp.space.dtu.dk/pub/DTU18/MSS_MATERIAL/PRESENTATIONS/DTU18MSS-V2.pdf

Arya, S. P. S. (1973). Contribution of form drag on pressure ridges to the air stress on Arctic ice. *Journal of Geophysical Research*, *78*(30), 7092–7099. https://doi.org/10.1029/jc078i030p07092

Bourke, R. H., & McLaren, A. S. (1992). Contour mapping of Arctic basin ice draft and roughness parameters. *Journal of Geophysical Research*, *97*(C11), 17715–17728. https://doi.org/10.1029/92JC01857

Castellani, G., Lupkes, C., Hendricks, S., & Gerdes, R. (2014). Variability of Arctic sea ice topography and its impact on the atmospheric surface drag. *Journal of Geophysical Research: Oceans*, *119*(10), 6743–6762. https://doi.org/10.1002/2013jc009712

Davis, N. R., & Wadhams, P. (1995). A statistical analysis of Arctic pressure ridge morphology. *Journal of Geophysical Research*, *100*(C6), 10915–10925. https://doi.org/10.1029/95JC00007

Dierking, W. (1995). Laser profiling of the ice surface topography during the Winter Weddell Gyre Study 1992. *Journal of Geophysical Research*, *100*(C3), 4807–4820. https://doi.org/10.1029/94JC01938

Duncan, K., & Farrell, S. (2022). ICESat-2 Arctic Sea Ice Surface topography from the University of Maryland-Ridge Detection Algorithm: April 2019, 2020, and 2021 (Version 1) [Dataset]. Zenodo. https://doi.org/10.5281/zenodo.6772544 .

Duncan, K., & Farrell, S. L. (2020). High-resolution sea ice topography from ICESat-2. In *Earth and Space Science Open Archive* (Vol. *1*). https://doi.org/10.1002/essoar.10505000.1

Duncan, K., Farrell, S. L., Connor, L. N., Richter-Menge, J., & Dominguez, R. (2018). High-resolution airborne observations of sea ice pressure-ridge sail height. *Annals of Glaciology*, *59*(76pt2), 137–147. https://doi.org/10.1017/aog.2018.2

Eicken, H., Grenfell, T. C., Perovich, D. K., Richter-Menge, J. A., & Frey, K. (2004). Hydraulic controls of summer Arctic pack ice albedo. *Journal of Geophysical Research*, *109*(C8), C08007. https://doi.org/10.1029/2003JC001989

Farrell, S. L., Duncan, K., Buckley, E. M., Richter-Menge, J., & Li, R. (2020). Mapping sea ice surface topography in high fidelity with ICESat-2. *Geophysical Research Letters*, *47*(21), e2020GL090708. https://doi.org/10.1029/2020GL090708

Haas, C., Lobach, J., Hendricks, S., Rabenstein, L., & Pfaffling, A. (2009). Helicopter-borne measurements of sea ice thickness, using a small and lightweight, digital EM system. *Journal of Applied Geophysics*, *67*(3), 234–241. https://doi.org/10.1016/j.jappgeo.2008.05.005

Hibler, W. D., III, Weeks, W. F., & Mock, S. J. (1972). Statistical aspects of sea-ice ridge distributions. *Journal of Geophysical Research*, *77*(30), 5954–5970. https://doi.org/10.1029/jc077i030p05954

Hibler, W. D., Mock, S. J., & Tucker, W. B. (1974). Classification and variation of sea ice ridging in the western Arctic basin. *Journal of Geophysical Research*, *79*(18), 2735–2743. https://doi.org/10.1029/jc079i018p02735

Hunke, E., Lipscomb, W., & Turner, A. (2010). Sea-ice models for climate study: Retrospective and new directions. *Journal of Glaciology*, *56*(200), 1162–1172. https://doi.org/10.3189/002214311796406095

Krabill, W. B., Abdalati, W., Frederick, E. B., Manizade, S. S., Martin, C. F., Sonntag, J. G., et al. (2002). Aircraft laser altimetry measurement of elevation changes of the Greenland ice sheet: Technique and accuracy assessment. *Journal of Geodynamics*, *34*(3–4), 357–376. https://doi.org/10.1016/s0264-3707(02)00040-6

Kwok, R., Kacimi, S., Markus, T., Kurtz, N. T., Studinger, M., Sonntag, J. G., et al. (2019). ICESat-2 surface height and sea ice freeboard assessed with ATM lidar acquisitions from Operation IceBridge. *Geophysical Research Letters*, *46*(20), 11228–11236. https://doi.org/10.1029/2019GL084976

Kwok, R., Markus, T., Kurtz, N. T., Petty, A. A., Neumann, T. A., Farrell, S. L., et al. (2019). Surface height and sea ice freeboard of the Arctic Ocean from ICESat-2: Characteristics and early results. *Journal of Geophysical Research: Oceans*, *124*(10), 6942–6959. https://doi.org/10.1029/2019JC015486

Kwok, R., Petty, A., Cunningham, G., Markus, T., Hancock, D., Ivanoff, A., & the ICESat-2 Science Team. (2021). *ATLAS/ICESat-2 L3A Sea Ice Height, Version 5. NASA Distributed Active Archive Center*. National Snow and Ice Data Center. https://doi.org/10.5067/ATLAS/ATL07.005

Lowry, R. T., & Wadhams, P. (1979). On the statistical distribution of pressure ridges in sea ice. *Journal of Geophysical Research*, *84*(C5), 2487–2494. https://doi.org/10.1029/JC084iC05p02487

MacGregor, J. A., Boisvert, L. N., Medley, B., Petty, A. A., Harbeck, J. P., Bell, R. E., et al. (2021). The scientific legacy of NASA's Operation IceBridge. *Reviews of Geophysics*, *59*(2), e2020RG000712. https://doi.org/10.1029/2020RG000712

Magruder, L. A., Brunt, K. M., & Alonzo, M. (2020). Early ICESat-2 on-orbit geolocation validation using ground- based corner cube retro-reflectors. *Remote Sensing*, *12*(21), 3653. https://doi.org/10.3390/rs12213653

Markus, T., Neumann, T., Martino, A., Abdalati, W., Brunt, K., Csatho, B., et al. (2017). The Ice, Cloud, and Land Elevation Satellite-2 (ICESat-2): Science requirements, concept, and implementation. *Remote Sensing of Environment*, *190*, 260–273. https://doi.org/10.1016/j.rse.2016.12.029

Martin, T., Tsamados, M., Schroeder, D., & Feltham, D. (2016). The impact of variable sea ice roughness on changes in Arctic Ocean surface stress: A model study. *Journal of Geophysical Research: Oceans*, *121*(3), 1931–1952. https://doi.org/10.1002/2015JC011186

Neumann, T. A., Brenner, A., Hancock, D., Robbins, J., Saba, J., Harbeck, K., et al. (2021). *ATLAS/ICESat-2 L2A Global Geolocated Photon Data, Version 5. NASA Distributed Active Archive Center*. National Snow and Ice Data Center. https://doi.org/10.5067/ATLAS/ATL03.005

Neumann, T. A., Martino, A. J., Markus, T., Bae, S., Bock, M. R., Brenner, A. C., et al. (2019). The Ice, Cloud, and Land Elevation Satellite–2 Mission: A global geolocated photon product derived from the advanced topographic laser altimeter system. *Remote Sensing of Environment*, *233*, 111325. https://doi.org/10.1016/j.rse.2019.111325

Newman, T., Farrell, S. L., Richter-Menge, J., Connor, L. N., Kurtz, N. T., Elder, B. C., & McAdoo, D. (2014). Assessment of radar-derived snow depth over Arctic sea ice. *Journal of Geophysical Research: Oceans*, *119*(12), 8578–8602. https://doi.org/10.1002/2014JC010284

Parmerter, R. R., & Coon, M. D. (1972). Model of pressure ridge formation in sea ice. *Journal of Geophysical Research*, *77*(33), 6565–6575. https://doi.org/10.1029/JC077i033p06565

Perovich, D., Meier, W., Tschudi, M., Farrell, S., Hendricks, S., Gerland, S., et al. (2019). Sea ice. In J. Richter-Menge, M. L. Druckenmiller, & M. Jeffries (Eds.), *Arctic Report Card 2019*. Retrieved from http://www.arctic.noaa.gov/Report-Card

Roberts, A. F., Hunke, E. C., Kamal, S. M., Lipscomb, W. H., Horvat, C., & Maslowski, W. (2019). A variational method for sea ice ridging in Earth system models. *Journal of Advances in Modeling Earth Systems*, *11*(3), 771–805. https://doi.org/10.1029/2018MS001395

Strub-Klein, L., & Sudom, D. (2012). A comprehensive analysis of the morphology of first-year sea ice ridges. *Cold Regions Science and Technology*, *82*, 94–109. https://doi.org/10.1016/j.coldregions.2012.05.014

Studinger, M. (2013). *IceBridge ATM L1B Elevation and Return Strength, Version 2 (ILATM1B)*. NASA Distributed Active Archive Center, National Snow and Ice Data Center. https://doi.org/10.5067/19SIM5TXKPGT

Tan, B., Li, Z., Lu, P., Haas, C., & Nicolaus, M. (2012). Morphology of sea ice pressure ridges in the northwestern Weddell Sea in winter. *Journal of Geophysical Research*, *117*(C6), C06024. https://doi.org/10.1029/2011JC007800

Timco, G. W., & Burden, R. P. (1997). An analysis of the shapes of sea ice ridges. *Cold Regions Science and Technology*, *25*(1), 65–77. https://doi.org/10.1016/S0165-232X(96)00017-1

Tsamados, M., Feltham, D. L., Schroeder, D., Flocco, D., Farrell, S. L., Kurtz, N., et al. (2014). Impact of atmospheric and oceanic form drag on simulations of Arctic sea ice. *Journal of Physical Oceanography*, *44*, 1329–1353. https://doi.org/10.1175/JPO-D-13-0215.1

Tschudi, M., Meier, W. N., Stewart, J. S., Fowler, C., & Maslanik, J. (2019). *EASE-Grid Sea Ice Age, Version 4. April 2019, 2020, and 2021 [accessed August 2, 2022]*. NASA Distributed Active Archive Center, National Snow and Ice Data Center. https://doi.org/10.5067/UTAV7490FEPB

Tschudi, M. A., Meier, W. N., & Stewart, J. S. (2020). An enhancement to sea ice motion and age products at the National Snow and Ice Data Center (NSIDC). *The Cryosphere*, *14*(5), 1519–1536. https://doi.org/10.5194/tc-14-1519-2020

Wadhams, P., & Doble, M. J. (2008). Digital terrain mapping of the underside of sea ice from a small AUV. *Geophysical Research Letters*, *35*(1), L01501. https://doi.org/10.1029/2007GL031921

Wadhams, P., & Toberg, N. (2012). Changing characteristics of arctic pressure ridges. *Polar Science*, *6*(1), 71–77. https://doi.org/10.1016/j.polar.2012.03.002

Wadhams, P., Tucker, W. B., III, Krabill, W. B., Swift, R. N., Comiso, J. C., & Davis, N. R. (1992). Relationship between sea ice freeboard and draft in the Arctic Basin, and implications for ice thickness monitoring. *Journal of Geophysical Research*, *97*(C12), 20325–20334. https://doi.org/10.1029/92jc02014

World Meteorological Organization. (1970). *Sea ice nomenclature: Terminology, codes and illustrated glossary, WMO/OMM/BMO 259, TP145*. World Meteorological Organization. Retrieved from https://www.jcomm.info/components/com_oe/oe.php?task=download%26id=27226%26version=March%202014%26lang=1%26format=1